

Bridging Implicit and Explicit Geometric Transformations for Single-Image View Synthesis

Byeongjun Park^{1*} Hyojun Go^{2*} Changick Kim^{1†}

¹School of Electrical Engineering, KAIST ²Riid

Abstract

Creating novel views from a single image has achieved tremendous strides with advanced autoregressive models. Although recent methods generate high-quality novel views, synthesizing with only one explicit or implicit 3D geometry has a trade-off between two objectives that we call the “seesaw” problem: 1) preserving reprojected contents and 2) completing realistic out-of-view regions. Also, autoregressive models require a considerable computational cost. In this paper, we propose a single-image view synthesis framework for mitigating the seesaw problem. The proposed model is an efficient non-autoregressive model with implicit and explicit renderers. Motivated by characteristics that explicit methods well preserve reprojected pixels and implicit methods complete realistic out-of-view region, we introduce a loss function to complement two renderers. Our loss function promotes that explicit features improve the reprojected area of implicit features and implicit features improve the out-of-view area of explicit features. With the proposed architecture and loss function, we can alleviate the seesaw problem, outperforming autoregressive-based state-of-the-art methods and generating an image ≈ 100 times faster. We validate the efficiency and effectiveness of our method with experiments on RealEstate10K and ACID datasets.

1 Introduction

Single-image view synthesis is the task of generating novel view images from a given single image [5, 19, 24, 40–42, 50, 53, 57]. It can enable the movement of the camera from a photograph and bring an image to 3D, which are significant for various computer vision applications such as image editing and animating. To perform the realistic single-image view synthesis in these applications, we can expect that the novel view image has to consist of existing objects and unseen new objects from the reference viewpoint. Therefore, for high-quality novel views, the following two goals should be considered: 1) preserving 3D transformed seen contents of a single reference image and 2) generating semantically compatible pixels for filling the unseen region. To achieve two goals, explicit and implicit methods have been proposed.

With the recent success of differentiable geometric transformation methods [2, 32], explicit methods [5, 18, 24, 53, 60] leverage such 3D inductive biases to guide the view synthesis network to preserve 3D transformed contents, and various generative models are applied to complete the unseen regions. Explicit methods can produce high-quality novel view images in small view changes, where the content of the reference viewpoint still occupies a large portion. However, for large view changes, the image quality is degraded due to a lack of ability to generate pixels of the unseen region. To deal with this problem, outpainting with the autoregressive model is exploited to fill unseen regions [41], but generating photo-realistic images remains a challenge for explicit methods.

*Both authors have contributed equally to this work.

†Corresponding Author.

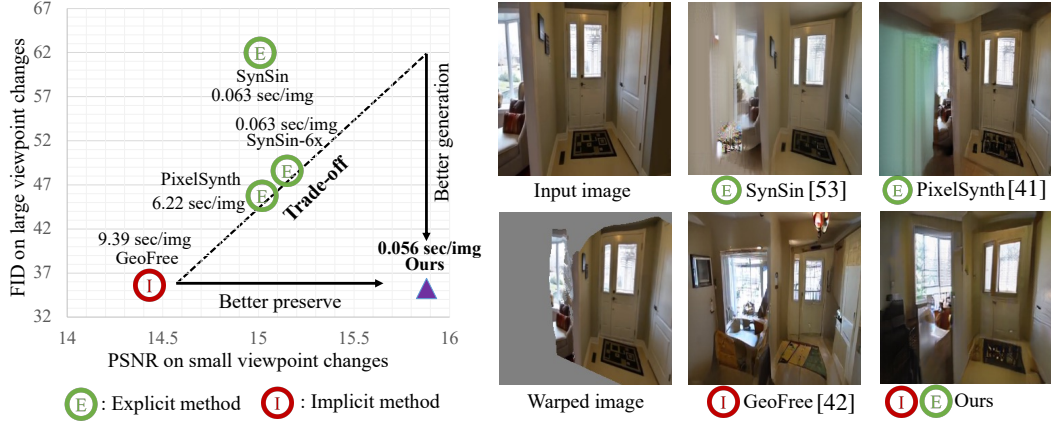


Figure 1: **Seesaw problem of explicit and implicit methods.** Explicit methods well preserve warped contents but sacrifice to fill unseen pixels (\uparrow PSNR on small view change, \uparrow FID on large view change). Implicit methods amply fill unseen pixels but fall short of preserving seen contents (\downarrow PSNR on small view change, \downarrow FID on large view change). Our proposed framework alleviates this seesaw problem and generates an image faster than the state-of-the-art methods.

On the other side, implicit methods [40, 42, 49] less enforce 3D inductive biases and let the model learn the required 3D geometry for view synthesis. Based on the powerful autoregressive transformer [11], recent implicit methods learn the 3D geometry from a reference image and camera parameters. Implicitly learned 3D geometry allows the model to synthesize diverse and realistic novel view images but fails to preserve the reprojected contents since they reduce 3D inductive biases.

To sum up, previous single-image view synthesis methods suffer from a trade-off between two objectives: 1) preserve seen contents and 2) generate semantically compatible unseen regions. Figure 1 shows an apparent trade-off that explicit methods well preserve seen contents with sacrificing the generation of unseen regions and vice versa for implicit methods. Here, we call this trade-off the *seesaw problem* and emphasize the need for combining solid points of explicit and implicit methods.

Moreover, recent methods often depend on autoregressive models, which generate individual pixels sequentially. Sequential generation causes too slower view synthesis than non-autoregressive methods, limiting their application areas, such as image animating in real-time. Therefore, we refocus on a fast and efficient non-autoregressive model for single view synthesis.

In this paper, we present a non-autoregressive framework for alleviating the seesaw problem. Our approach aims to design the architecture and loss functions. We design two parallel render blocks which explicitly or implicitly learn geometric transformations from point cloud representations. To bridge explicit and implicit transformations, we propose a novel loss function that motivates explicit features improve seen pixels of implicit features and implicit features improve unseen pixels of explicit features. Interestingly, we observe that proposed loss makes two renderers embed discriminative features and allow the model to use both renderers in a balanced way to create novel views. With the proposed architecture and the loss function, we can merge the pros of both explicit and implicit methods, alleviating the seesaw problem. As a result, our non-autoregressive framework can better preserve seen contents, better complete unseen pixels, and generate images ≈ 100 times faster than autoregressive methods. We validate the efficiency and effectiveness of our framework with experiments on the indoor dataset RealEstate10K [61] and the outdoor dataset ACID [24].

2 Related Works

Novel view synthesis Given multiple images from different viewpoints of a scene, novel view synthesis aims to generate novel view images. Traditionally, multi-view geometry is utilized for synthesizing novel viewpoints [4, 6, 7, 14, 22, 44, 62]. Recently, deep neural networks have been used to rendering [16, 29, 30, 33] and several representation for view synthesis such as multi-plane image [12, 48, 61], point cloud [1], depth [47], radiance field [31, 52, 58] and voxel [26, 34, 46].

Single-image view synthesis is more challenging than general novel view synthesis since a single input image is only available [5, 19, 24, 40–42, 50, 53, 57]. Explicit methods directly inject 3D

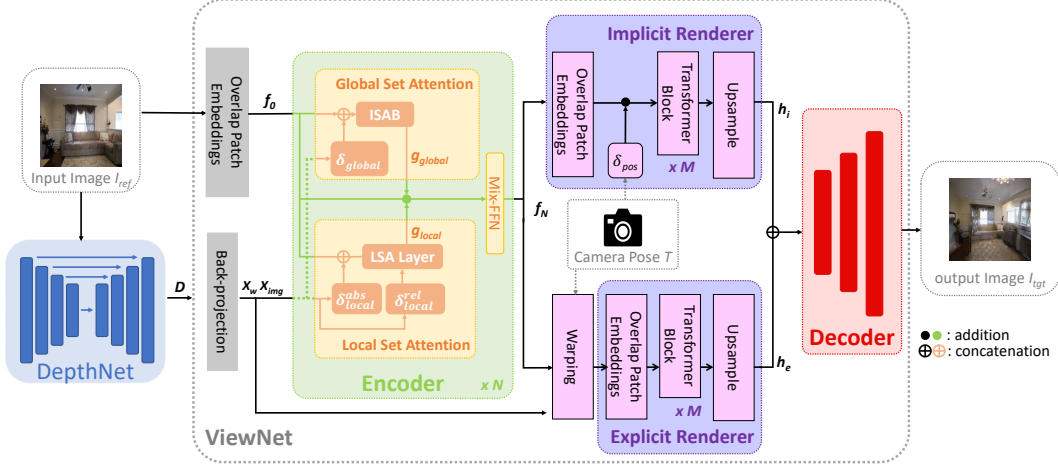


Figure 2: **An overview of network architecture.** Our network takes a reference image I_{ref} and a relative camera pose T as inputs. The depth estimation network (DepthNet) first predicts a depth map D , and the view synthesis network (ViewNet) generates a target image I_{tgt} from I_{ref} , D and T . Specifically, D is used for calculating the 3D world coordinate X_w and the normalized image coordinate X_{img} at the reference viewpoint, which are passed through various positional encoding layers in the encoder (e.g., δ_{global} , δ_{local}^{abs} and δ_{local}^{rel}) to provide the scene structure representations. Encoded features f_N are then transformed by both Implicit Renderer and Explicit Renderer with T . Finally, two transformed feature map, h_i and h_e , are concatenated to generate I_{tgt} by the decoder.

inductive biases into models. For example, SynSin [53] uses 3D point cloud features with estimated depth from the model, projects to novel viewpoints, and refines unseen pixels with recent generative models [3]. SynSin works well in small viewpoint changes but degrades in large viewpoint changes due to the lack of generating unseen pixels. To deal with this problem, PixelSynth [41] exploits the autoregressive outpainting model [39] with 3D point cloud representation. Despite using the slow autoregressive model, it cannot generate unseen pixels well. For an implicit method, Rombach *et al.* [42] propose a powerful autoregressive transformer. By less enforcing 3D inductive biases, this approach can generate realistic view synthesis and complete the unseen region without explicit 3D geometry. However, its inference time is long due to the autoregressive model, and it fails to preserve seen contents of a reference image. We bridge these implicit and explicit methods as a non-autoregressive architecture, which can outperform autoregressive approaches with fast inference.

Transformer for point cloud The transformer and self-attention have brought a breakthrough in natural language processing [8, 51] and computer vision [10]. Inspired by this success, transformer and self-attention networks have been widely applied for point cloud recognition tasks and achieved remarkable performance gain. Early methods utilize global attention for all of the point clouds, resulting in a large amount of computation and inapplicable for large-scale 3D point cloud [25, 55, 56]. Lee *et al.* [21] propose the SetTransformer module suitable for point cloud due to permutation-invariant, which uses inducing point methods and reduces computational complexity from quadratic to linear in the number of elements. Also, local attention methods is utilized to enable scalability [15, 35, 59]. Notably, among local attention methods, Fast Point Transformer [35] which uses voxel hashing-based architecture, achieves both remarkable performance and computational efficiency. Global attention may dilute important content by excessive noises as most neighbors are less relevant, and local attention may not have sufficient context due to their scope. Therefore, Our approaches use both global and local attention to deal with 3D point cloud representation.

3 Methodology

Given a reference image I_{ref} and a relative camera pose T , the goal of single-image view synthesis is to create a target image I_{tgt} with keeping visible contents of I_{ref} and completing realistic out-of-view pixels. To achieve this, we focus on mitigating the seesaw problem between explicit and implicit methods in terms of the network architecture and the loss function. Figure 2 describes an overview of our network architecture. The network consists of two sub-networks, the depth estimation network

(**DepthNet**) and the view synthesis network (**ViewNet**). Note that the pre-trained DepthNet generates depth map D , which is used for ViewNet to synthesize the photo-realistic I_{tgt} .

3.1 Depth Estimation Network (DepthNet)

We train the depth estimation network for explicit 3D geometry since ground-truth depths are not available. Following Monodepth2 [13], our DepthNet is trained in a self-supervised manner from monocular video sequences. Because a ground-truth relative pose between images is available, we substitute the pose estimation network with the ground-truth relative pose. Then, we train the network on reprojection losses and smoothness losses with auto-masking in their work. After training DepthNet, we fix it during training ViewNet.

3.2 View Synthesis Network (ViewNet)

We design a simple view synthesis network built on architectural innovations of recent transformer models. Specifically, we exploit 3D point cloud representation to consider the relationship between the geometry-aware camera pose information and the input image.

Encoder The encoder aims to extract scene representations from a feature point cloud of a reference image. To deal with point clouds, we design a Global and Local Set Attention (GLSA) block which simultaneously extracts overall contexts and detailed semantics. For efficient input size of transformers, $I_{ref} \in \mathbb{R}^{H \times W \times 3}$ is encoded into $f_0 \in \mathbb{R}^{\frac{H}{4} \times \frac{W}{4} \times C}$ by an overlapping patch embedding [54], where C denotes the channel dimension. Then, the homogeneous coordinates p of a pixel in f_0 are mapped into normalized image coordinates X_{img} as $X_{img}(p) = K_{\downarrow}^{-1}p$, where K_{\downarrow} denotes the camera intrinsic matrix of f_0 . Finally, 3D world coordinates of p are calculated with depth map D as $X_w(p) = D(p)X_{img}(p)$. Our encoder architecture is N stacked GLSA block, and i -th GLSA block receives f_{i-1} , X_{img} and X_w and outputs f_i with Mix-FFN [54].

Global Set Attention. We utilize Induced Set Attention Block (ISAB) [21] to extract global set attention between the feature point clouds. With positional encoder δ_{global} and vector concatenation operator \oplus , the global attention of i -th GLSA block is represented as:

$$g_{global}^i(p) = ISAB(f_i(p) \oplus \delta_{global}(X_w(p))). \quad (1)$$

Local Set Attention. We use a modified Lightweight Self-Attention (LSA) layer [35] for the set attention in $r \times r$ local window of each pixel point. Unlike the decomposing relative position of voxels in [35], we decompose the relative position of 3D world coordinates between neighbor pixels using normalized image coordinates as:

$$X_w(p) - X_w(q) = (X_w(p) - X_{img}(p)) - (X_w(q) - X_{img}(q)) + (X_{img}(p) - X_{img}(q)), \quad (2)$$

where $q \in \mathcal{N}(p)$ is a neighbor set of homogeneous coordinates in a $r \times r$ window of p . With decomposition in Eq. 2, we can divide the relative positional encoding into an continuous positional encoding δ_{local}^{abs} and a discretized positional encoding δ_{local}^{rel} . Then, the computation procedures for local set attention g_{local}^i of i -th GLSA block is similar to LSA layer as:

$$\begin{aligned} l_{local}^i(p) &= f_i(p) \oplus \delta_{local}^{abs}(X_w(p) - X_{img}(p)), \\ g_{local}^i(p) &= \sum_{q \in \mathcal{N}(p)} S_C(\psi(l_{local}^i(p)), \delta_{local}^{rel}(X_{img}(p) - X_{img}(q))) \phi(l_{local}^i(q)), \end{aligned} \quad (3)$$

where ψ and ϕ are MLP-layers, and $S_C(a, b) = \frac{a \cdot b}{\|a\| \|b\|}$ computes the cosine similarity between a and b . As pixel coordinates of p and q are all integer, the encoding of $X_{img}(p) - X_{img}(q)$ is hashed over $r^2 - 1$ values, resulting in a space complexity reduction from $\mathcal{O}(HW \cdot r^2 \cdot C)$ to $\mathcal{O}(HW \cdot C) + \mathcal{O}(r^2 \cdot C)$.

Rendering Module Given the scene representations of the reference image, the rendering module learns 3D transformation from the reference viewpoint to the target viewpoint. Motivated by our observations of implicit and explicit methods, we design an Explicit Renderer(ER) and an Implicit Renderer(IR) connected in parallel to bypass the seesaw problem. The structure of the two renderers is similar; they consist of an overlapping patch embedding, GPT architecture [37] and ResNet blocks with upsampling layers. Note that the overlapping patch embedding and upsampling layers are

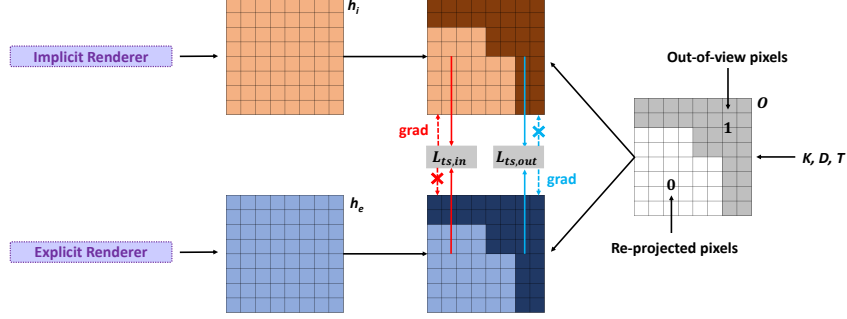


Figure 3: **An overview of our transformation similarity loss.** Two transformed features, h_i and h_e , are complemented each other by the transformation similarity loss. Specifically, we first derive out-of-view mask \mathbf{O} from K , D and T . By using \mathbf{O} , two transformation similarity loss, i.e., $L_{ts,in}$ and $L_{ts,out}$, are applied to encourage the discriminability of h_i and h_e , respectively. To guide the another renderer as intended, we allow the back-propagated gradients of $L_{ts,in}$ only to the reprojected regions of h_i , and those of $L_{ts,out}$ only to the out-of-view regions of h_e .

designed for downsampling and upsampling the input feature with the factor of 4, respectively. The major difference between the two renderers is how the relative camera pose T is used for the geometric transformation.

Explicit Renderer (ER). Given the rotation matrix R and translation vector t of relative camera pose T , p can be reprojected to the homogeneous coordinates of target viewpoint p' as $p' = K_{\downarrow} R X_w(p) + t$. The output of encoder f_N is warped by splatting operation [32] with optical flow from p to p' . Then, warped f_N goes through the explicit renderer to produce explicit feature map h_e .

Implicit Renderer (IR). Unlike the explicit renderer, the implicit renderer uses the camera parameter itself. Instead of embedding 3×4 camera extrinsic matrix, we use independent 7 parameters to embed pose information; Translation vector t and axis-angle notation $(\frac{\mathbf{u}}{\|\mathbf{u}\|}, \theta)$ to parameterize rotation matrix R . We use a positional encoding layer δ_{pos} to embed these parameters and add them to the input of the transformer block. f_N passes through the implicit renderer and outputs implicit feature map h_i . Please refer to the supplementary materials for details to compute the axis-angle notation.

Decoder Two feature maps from *ER* and *IR*, which are denoted as h_e and h_i , are then concatenated before the decoder. We use a simple CNN-based decoder by gradually upsampling the concatenated feature map with four ResNet blocks. Instead of generating pixels in an auto-regressive manner, we directly predict all pixels in the one-path, resulting in more than 110 times faster than the state-of-the-art autoregressive methods [40–42] in generating images.

3.3 Loss Design for ViewNet

Following the previous single-image view synthesis methods [41, 53], we also use the ℓ_1 -loss, perceptual loss [36] and adversarial loss to learn the network. Specifically, we compute ℓ_1 -loss and perceptual loss between I_{tgt} and the ground-truth image I_{gt} at the target viewpoint. Also, we use the global and local discriminators [20] with a Projected GAN [43] structure and a hinge loss [23]. We observe that our methods improve the generation performance even through these simple network structural innovations. Furthermore, we introduce a transformation similarity loss L_{ts} to complement two output feature maps h_e and h_i .

Transformation Similarity Loss As an extension of the existing seesaw problem, h_e may have better discriminability than h_i in reprojected regions, conversely, h_i has better delineation of out-of-view regions than h_e . Therefore, as shown in Fig. 3, we design the transformation similarity loss between h_e and h_i , expecting that h_i learns to keep reprojected image contests, and h_e also learn to generate realistic out-of-view pixels. Specifically, we use a negative cosine similarity function

S_c for calculating the similarity between two feature maps, and the transformation similarity loss $L_{ts} = \lambda_{in} L_{ts,in} + \lambda_{out} L_{ts,out}$ is formulated as:

$$\begin{aligned} L_{ts,in} &= -\frac{1}{\sum_p (1 - \mathbf{O}(p))} \sum_p (1 - \mathbf{O}(p)) \cdot S_c(h_i(p), \text{detach}(h_e(p))), \\ L_{ts,out} &= -\frac{1}{\sum_p \mathbf{O}(p)} \sum_p \mathbf{O}(p) \cdot S_c(\text{detach}(h_i(p)), h_e(p)), \end{aligned} \quad (4)$$

where $\mathbf{O}(p) \in \mathbb{R}^{\frac{H}{4} \times \frac{W}{4}}$ denotes an out-of-view mask which is derived from the depth map D and the relative camera pose T . Note that, without detach operations, our transformation similarity loss performs the same as a simple negative cosine similarity loss between two feature maps. Thus, we detach gradients back-propagated from $L_{ts,in}$ to h_e and gradients from $L_{ts,out}$ to h_i , because the detach operation allows the components of L_{ts} to be applied to the intended area.

Final Learning Objective Taken together, our ViewNet is trained on the weighted sum of a ℓ_1 -loss L_{ℓ_1} , a perceptual loss L_c , an adversarial loss L_{adv} and a transformation similarity loss L_{ts} . The total loss is then $L = L_{\ell_1} + \lambda_c L_c + \lambda_{adv} L_{adv} + L_{ts}$. We fix $\lambda_c = 1$ and $\lambda_{adv} = 0.1$ for all experiments.

Table 1: **Types of baselines and our method.** Note that InfNat [24] varies according to the number of steps, so we mark it as \triangle .

| Types | Methods | | | | | | | |
|----------------|--------------------------------|---------------------|--------------|--------------|-----------------|--------------|------------------|--------------|
| | Tatarchenko <i>et al.</i> [49] | Viewappearance [60] | SynSin [53] | InfNat [24] | PixelSynth [41] | GeoFree [42] | LookOutside [40] | Ours |
| Explicit | \checkmark | \checkmark | \checkmark | \checkmark | \checkmark | \checkmark | \checkmark | \checkmark |
| Implicit | \checkmark | \times | \times | \times | \times | \times | \times | \checkmark |
| Autoregressive | \times | \times | \times | \triangle | \checkmark | \checkmark | \checkmark | \times |

4 Experimental Results

4.1 Experimental Settings

We now describe experimental settings, and please refer to the supplementary materials for further details about datasets, baselines, and our network architecture.

Dataset We used two standard datasets, *RealEstate10K* [61] and *ACID* [24], which are a collection of videos mostly captured in indoor and outdoor scenes, respectively. We divided train and test sequences as in [42].

Baselines To validate the effectiveness of our framework, we compared our method to previous single-image view synthesis methods : Tatarchenko *et al.* [49], Viewappearance [60], Synsin [53], InfNat [24], PixelSynth [41], GeoFree [42] and LookOutside [40]. Table 1 briefly shows whether each method is an explicit, implicit, and autoregressive model. Compared to previous methods, we use both explicit and implicit geometric transformations without an autoregressive model.

Evaluation Details Because explicit and implicit methods are respectively advantageous in small view change and large view change, methods should be evaluated on several sizes of viewpoint changes for a fair comparison. Therefore, we used a ratio of out-of-view pixels over all pixels to quantify view changes, resulting in three splits are categorized into *small* (20-40%), *medium* (40-60%) and *large* (60-80%). Since evaluation datasets do not have ground-truth depth maps, we used depth maps from our pre-trained DepthNet to derive the ratio of out-of-view mask pixels. Finally, we used randomly selected 1,000 image pairs for each test split.

We use PSNR on the small split and FID [17] on the medium and large split as evaluation metrics. PSNR is a traditional metric for comparing images, which is widely used to evaluate *consistency*. Nevertheless, PSNR is a poor metric to verify the image quality on large viewpoint changes [41, 42]. Still, it can be a good metric for evaluating the preservation of reprojected pixels on small view changes. Therefore, we use PSNR on the small split to evaluate the ability to preserve seen contents. For evaluating images quality of view synthesis, FID is widely used [41, 42, 53]. Especially in the medium and large split with many out-of-view pixels, FID indicates how well the model fills out-of-view pixels and generates realistic images. We use the PSNR and FID of specific splits as evaluation metrics, but we report the PSNR and FID of all splits to show the overall trend.

Table 2: **Quantitative results on RealEstate10K and ACID.** Image quality is measured by PSNR and FID for three types of view changes, i.e., *Small*, *Medium* and *Large*. Furthermore, we show the average performance over all view changes at the end. For both datasets, best results in each metric are in **bold**, and second best are underlined.

| Dataset | Methods | Small | | Medium | | Large | | Average | |
|--------------------|--------------------------------|-----------------|------------------|-----------------|------------------|-----------------|------------------|-----------------|------------------|
| | | PSNR \uparrow | FID \downarrow | PSNR \uparrow | FID \downarrow | PSNR \uparrow | FID \downarrow | PSNR \uparrow | FID \downarrow |
| RealEstate10K [61] | Tatarchenko <i>et al.</i> [49] | 11.12 | 258.75 | 10.90 | 248.55 | 10.80 | 249.24 | 10.94 | 252.18 |
| | Viewappearance [60] | 12.51 | 142.93 | 12.79 | 110.84 | 12.44 | 147.27 | 12.58 | 133.68 |
| | SynSin [53] | 15.38 | 41.75 | 14.88 | 43.06 | 13.96 | 61.67 | 14.74 | 48.83 |
| | SynSin-6x [53] | 15.17 | 33.72 | 14.99 | 37.28 | 14.26 | 48.29 | 14.81 | 39.76 |
| | PixelSynth [41] | 14.46 | 37.23 | 13.46 | 38.39 | 12.28 | 45.44 | 13.40 | 40.35 |
| | GeoFree [42] | 14.16 | 33.48 | 13.15 | 34.21 | 12.57 | 35.28 | 13.29 | 34.32 |
| | LookOutside [40] | 12.58 | 44.87 | 12.72 | 43.17 | 12.11 | 43.22 | 12.47 | 43.75 |
| | ours | 15.87 | 32.42 | 14.65 | 33.04 | 13.83 | 35.26 | 14.78 | 33.57 |
| ACID [24] | Tatarchenko <i>et al.</i> [49] | 14.43 | 148.19 | 14.20 | 151.24 | 14.34 | 150.47 | 14.32 | 149.97 |
| | Viewappearance [60] | 14.46 | 161.91 | 13.58 | 203.19 | 13.21 | 218.37 | 13.75 | 194.49 |
| | SynSin [53] | 17.48 | 55.64 | <u>16.49</u> | 75.88 | 16.87 | 79.04 | 16.95 | 70.19 |
| | InfNat [24] (1-step) | 15.94 | 64.32 | 14.40 | 90.80 | 13.65 | 106.28 | 14.66 | 87.13 |
| | InfNat [24] (5-step) | 15.16 | 64.48 | 14.79 | 71.52 | 14.90 | 65.45 | 14.95 | 67.15 |
| | PixelSynth [41] | 15.81 | 53.38 | 14.33 | 63.48 | 13.53 | 65.60 | 14.56 | 60.82 |
| | GeoFree [42] | 14.80 | 53.21 | 14.24 | 58.92 | 14.22 | 54.78 | 14.42 | 55.64 |
| | ours | 17.52 | 42.52 | 16.54 | 51.56 | 15.81 | 49.28 | 16.62 | 47.79 |

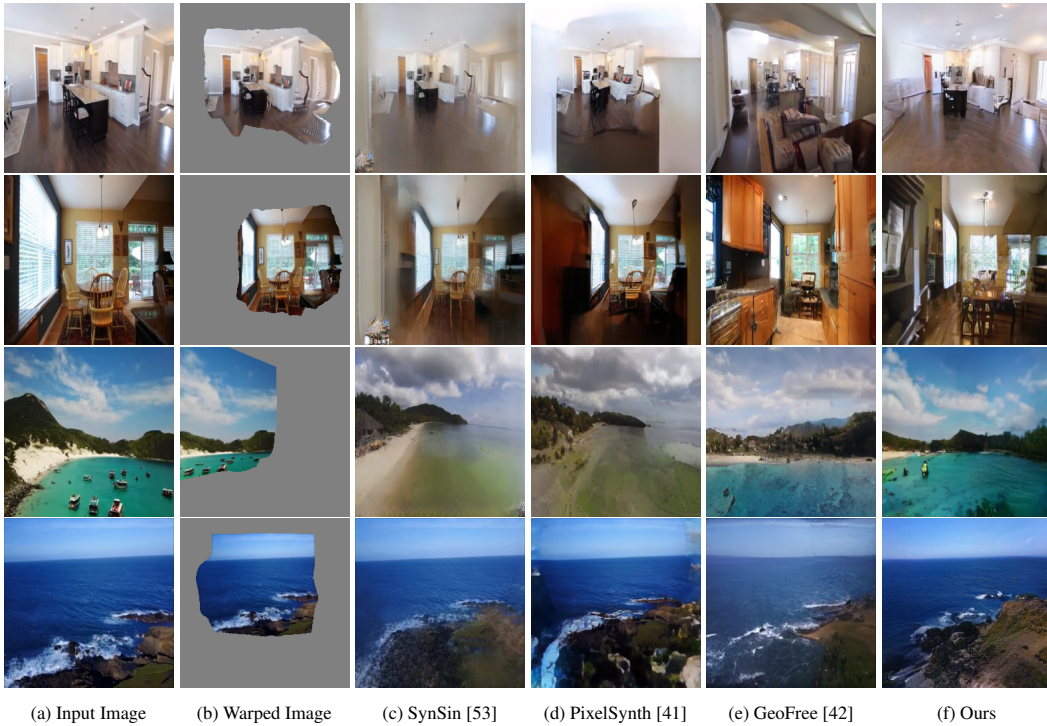


Figure 4: **Qualitative Results on RealEstate10K and ACID.** We compare baselines to our method. The top two rows are from RealEstate10K, and the bottom two rows are from ACID.

Implementation Details We first resized all images into a resolution of 256×256 , and normalized RGB value following [41, 53]. We trained DepthNet using a batch size 50 for 100k iterations and ViewNet using a batch size 32 for 150k iterations. Training takes about 3 days on 4 NVIDIA Geforce RTX 3090 GPUs. We used an AdamW [28] optimizer (with $\beta_1 = 0.5$ and $\beta_2 = 0.9$) and applied weight decay of 0.01. We first linearly increased the learning rate from 10^{-6} to $3 \cdot 10^{-4}$ during the first 1.5k steps, and then a cosine-decay learning rate schedule [27] was applied towards zero. In ViewNet, we used 8 GLSA blocks with local window size $r = 5$ and 6 transformer blocks in each renderer for all experiments.

4.2 Comparison to Baselines

We now compare our method with the state-of-the-art methods on RealEstate10K and ACID. Table 2 shows quantitative results for both datasets. The implicit method GeoFree [42] reports a lower

Table 3: Average inference time.

| Methods | SynSin | InfNat (5-step) | PixelSynth |
|--------------|---------|-----------------|------------|
| Time (s/img) | 0.063 | 1.14 | 6.22 |
| Methods | GeoFree | LookOutside | Ours |
| Time (s/img) | 9.39 | 22.15 | 0.056 |

Table 5: Ablation Study on the Set Attention.

| Set Attention | | Small | | Medium | | Large | |
|---------------|--------------|-----------------|------------------|-----------------|------------------|-----------------|------------------|
| g_{local} | g_{global} | PSNR \uparrow | FID \downarrow | PSNR \uparrow | FID \downarrow | PSNR \uparrow | FID \downarrow |
| ✓ | | 15.69 | 34.07 | 14.64 | 34.81 | 13.78 | 37.63 |
| | ✓ | 15.74 | 32.80 | 14.61 | 34.37 | 13.88 | 38.68 |
| ✓ | ✓ | 15.87 | 32.42 | 14.65 | 33.04 | 13.83 | 35.26 |

Table 4: Ablation study on L_{ts} .

| | Loss Type | | | | |
|------------------|-------------|-------------|--------------|----------------------|--------------|
| | no L_{ts} | $L_{ts,in}$ | $L_{ts,out}$ | L_{ts} (no detach) | L_{ts} |
| PSNR \uparrow | 14.47 | 14.62 | 14.73 | 14.59 | 14.78 |
| FID \downarrow | 40.45 | 38.05 | 36.95 | 40.44 | 33.57 |

Table 6: Ablation Study on hyperparameters of transformation similarity loss.

| Loss Weight | | Small | | Medium | | Large | |
|----------------|-----------------|-----------------|------------------|-----------------|------------------|-----------------|------------------|
| λ_{in} | λ_{out} | PSNR \uparrow | FID \downarrow | PSNR \uparrow | FID \downarrow | PSNR \uparrow | FID \downarrow |
| 0.1 | 1 | 15.78 | 33.95 | 14.65 | 34.10 | 13.81 | 37.11 |
| 10 | 1 | 15.48 | 37.46 | 14.39 | 37.46 | 13.56 | 40.69 |
| 1 | 0.1 | 15.46 | 34.98 | 14.37 | 37.51 | 13.64 | 39.81 |
| 1 | 10 | 15.70 | 35.03 | 14.54 | 35.57 | 13.77 | 38.43 |
| 1 | 1 | 15.87 | 32.42 | 14.65 | 33.04 | 13.83 | 35.26 |

FID in the medium and large split than explicit methods such as SynSin [53] and PixelSynth [41], but its PSNR of the small split is lower. This shows that previous methods are suffered from the seesaw problem. However, our method consistently achieves the highest PSNR in the small split on both datasets, which means our method better preserves reprojected contents than previous methods. Moreover, our method also achieves the lowest FID in all splits on both datasets, and this demonstrates that our method generates better quality images with filling compatible pixels regardless of view changes. As observed in [40, 41], we note that SynSin and its variant (i.e., SynSin-6x) often produce entirely gray images, resulting they still performing competitive results in PSNR of the medium and large split. Considering this, our method stably outperforms previous methods in all splits.

Also, qualitative results in Fig. 4 illustrate that the warped regions are well-preserved and invisible parts are well-completed in our method, whereas explicit methods do not generate realistic images, and an implicit method loses the semantic information of visible contents. Specifically, GeoFree [42] does not preserve the table in the first sample and the ships floating on the sea in the third sample. Also, explicit methods [41, 53] either make the entire out-of-view regions in one color or produce a less realistic view than our method.

We confirm that mitigating the seesaw problem by well-bridged explicit and implicit geometric transformations yields high-quality view synthesis, even acquiring a generation speed of about 110 times faster than the previous autoregressive models, as shown in Table 3. The fast generation of novel view images allows our method to be scalable to various real-time applications.

4.3 Ablation Study: Type of Set Attention

We design the global and local set attention block to simultaneously extract overall contexts and detailed semantics. Therefore, we conducted an ablation study on RealEstate10K [61] to verify each attention improves the performance of generating novel views. Table 5 shows the quantitative result for the type of set attention. Interestingly, our local set attention improves the performance relatively in large view changes, while our global set attention performs well on small view changes. From this result, we conjecture that local and global set attention are more useful for structural reasoning of out-of-view regions and 3D scene representation of reprojected regions, respectively. Also, significant performance improvement is achieved when both attentions are used.

4.4 Ablation Study: Transformation Similarity Loss

The transformation similarity loss L_{ts} is weighted combination of $L_{ts,in}$ and $L_{ts,out}$. To understand the effect of each component, we conducted ablation studies of transformation similarity loss on the RealEstate10K dataset. Table 4 reports the average PSNR and FID of our model by changing various components of L_{ts} . Results show that combining with gradient stopping operation, $L_{ts,in}$, and $L_{ts,out}$ achieves best results among the five variants. Also, either using $L_{ts,in}$ or $L_{ts,out}$ improves the performance and shows that guiding one renderer from the other renderer with the proposed loss function is effective. Notably, transformation similarity loss is not practical when the detach operation is not used. From this result, it is necessary to selectively guide unseen and seen regions by detaching the gradient.

We also performed an ablation study on balancing parameter λ_{in} and λ_{out} . Table 6 illustrates the results varying weight of L_{ts} . Results show that the case of $\lambda_{in} = 1, \lambda_{out} = 1$ performs best. As mentioned above, it seems essential to complement each other in a balanced way.

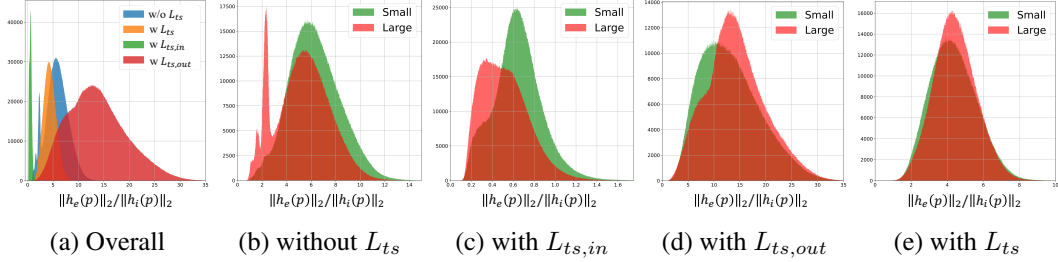


Figure 5: **Histogram of $\|h_e(p)\|_2 / \|h_i(p)\|_2$ on the small and large split of RealEstate10K dataset.**

4.5 Dependency Analysis between Implicit and Explicit Renderers

Our proposed architecture exploits the implicit and explicit renderer and mixes their outputs for decoding view synthesis results. To understand the dependency between two renderers, we analyze the norm of output feature maps. For a spatial position p , the norm ratio of two spatial features $\|h_e(p)\|_2 / \|h_i(p)\|_2$ can represent how much depends on the explicit feature $h_e(p)$ compared to implicit feature $h_i(p)$. For example, if the ratio is large, the model depends on the explicit renderer than the implicit renderer at position p . We compare histograms of the norm ratio by changing the components of L_{ts} and data splits as shown in Fig. 5.

Figure 5a depicts that using $L_{ts,out}$ and $L_{ts,in}$ tends to make the model more dependent on explicit and implicit features, respectively, compared to our method trained without L_{ts} . Furthermore, these tendencies are more apparent in difficult cases (i.e., large split) as shown in Fig. 5c–5d. From our observations, we conjecture that guiding only a specific renderer improves the discriminability of that renderer, resulting in the model depending on the improved renderer. Surprisingly, the model trained on combining all components of L_{ts} uses both renderers in a balanced way, and there is less bias in norm ratio even according to data splits as shown in Fig. 5e.

The effectiveness of our transformation similarity loss is confirmed by comparing it to our method that is trained without L_{ts} . Figure 5b shows that our model trained without L_{ts} has some outliers for large view changes despite there being less bias according to data splits. We observe these outliers are derived when the model fails to generate realistic out-of-view regions, especially in challenging settings, such as the network having to create novel views for both indoor and outdoor scenes, as shown in Fig. 6. We also confirm that our model trained with L_{ts} performs well even in extreme cases, informing that L_{ts} improves two renderers to embed discriminative features. Collectively, L_{ts} improves the discriminability of output features from two renderers and makes the behavior of the model stable, resulting in alleviating the seesaw problem.

5 Conclusion

We have introduced a single-image view synthesis framework by bridging explicit and implicit renderers. Despite using autoregressive models, previous methods still suffer from the seesaw problem since they use only one explicit or implicit geometric transformation. Thus, we design two parallel renderers to mitigate the problem and complement renderers with transformation similarity loss. Alleviating the seesaw problem allows the network to generate novel view images better than previous methods, even with a non-autoregressive structure. We note that the effectiveness of bridging two renderers can be applied in other tasks, such as extrapolation. We believe that our work can prompt refocusing on non-autoregressive architecture for single-image view synthesis.

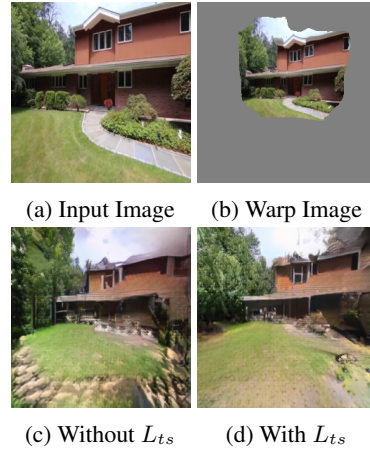


Figure 6: **Visual ablation study.** Without the transformation similarity loss, our model complete textured out-of-view regions but not realistic enough than our model trained with the transformation similarity loss.

Supplemental Materials

A Notations

Images and Feature maps:

| | |
|----------------|--|
| I_{ref} | Input image |
| I_{tgt} | Generated target image |
| I_{gt} | Ground-truth target image |
| D | The estimated Depth Map from DepthNet |
| f_i | The i -th output point feature of the encoder |
| l_{local}^i | The continuous positional encoded feature of the i -th LSA layer |
| g_{global}^i | The i -th global set attention of the encoder |
| g_{local}^i | The i -th local set attention of the encoder |
| h_i | The output feature map of the implicit renderer |
| h_e | The output feature map of the explicit renderer |
| O | The out-of-view mask |

Camera parameters and Coordinates:

| | |
|-----------------------------|--|
| K | Input camera intrinsic matrix for a resolution of $H \times W$ |
| T | Input relative camera pose matrix |
| R | The rotation matrix of T |
| t | The translation vector of T |
| $\mathbf{u}/\ \mathbf{u}\ $ | The normalized axis that is not changed by R |
| θ | The amount of rotated angle of R |
| X_{img} | A set of normalized image coordinates |
| X_w | A set of 3D world coordinates |
| $\mathcal{N}(p)$ | A set of neighbor homogeneous coordinates of p |

MLP-layers and Operations:

| | |
|-------------------|--|
| δ_{global} | A position encoding layer in ISAB |
| δ_{abs} | A continuous position encoding layer in LSA layer |
| δ_{local} | A discretized position encoding layer in LSA layer |
| δ_{rel} | A query projection layer in LSA layer |
| ψ | A value projection layer in LSA layer |
| ϕ | A positional encoding layer for camera parameters |
| δ_{pos} | A positional encoding layer for camera parameters |
| \oplus | A vector concatenation operation |
| $S_c(\cdot)$ | A cosine similarity operation |

B Experimental Details

B.1 Datasets

To select training image pairs from video clips in RealEstate10K [61] and ACID [24], our selection protocol proceeds similarly to the previous work [53]. However, we experimentally set selection limits that allow the network to learn both small and large view changes and exclude situations of entering different rooms. Specifically, we set the range of angle ($^\circ$), translation (m) and frame differences (frames) to $[10, 60]$, $[0, 3]$ and $[0, 100]$ for both datasets, respectively.

B.2 Baselines

SynSin [53] SynSin [53] uses a point cloud representation for single-image view synthesis. Similar to our method, it does not require any ground-truth 3D information and uses a differentiable point cloud renderer. The point cloud representation projected by the renderer is refined to generate novel view images. Since the official code is publicly available, we use it for implementation³. SynSin-6x, which is a variant of SynSin trained on large viewpoint changes, is introduced in [41]. For implementation of SynSin-6x, we adopt the official code of PixelSynth [41]⁴.

³<https://github.com/facebookresearch/synsin>

⁴<https://github.com/crockwell/pixelsynth>

PixelSynth [41] SynSin achieves remarkable view synthesis results in small viewpoint changes, but it fails to fill the unseen region of novel view images realistically. PixelSynth utilizes the outpainting strategy for supplementing the ability to complete the unseen region of SynSin. Although a slow autoregressive model is used for outpainting, PixelSynth still performs poorly in filling the out-of-view pixels. The official code is publicly available, and we utilize it for implementation ⁴.

GeoFree [42] With the powerful transformer and autoregressive model, GeoFree [42] shows that the model can learn the 3D transformation needed for the single-image view synthesis. Its view synthesis results are realistic, but it fails to maintain the seen contents. We adopt the official code for implementation ⁵.

Tatarchenko *et al.* [49] Tatarchenko *et al.* [49] use a convolutional neural network to predict an RGB image and a depth map for arbitrary viewpoint. We adopt the implementation of SynSin [53] ³.

Viewappearance [60] Viewappearance [60] predicts the flow and warps the reference image to the target view with this flow. For implementation, we used the implementation of SynSin [53] ³.

InfNat [24] Infinite Nature [24] focuses on nature scenes and generates a video from an image and a camera trajectory. InfNat uses a pretrained MiDAS [38] to estimate depth maps, and novel views are generated based on explicit geometric transformations. We evaluate the performance for 1-step (i.e., direct generation) and 5-step (i.e., gradual generation for target view). We adopt the official code for implementation ⁶.

LookOutside [40] Ren *et al.* [40] focus on long-term view synthesis with the autoregressive model. Novel views are generated time-sequentially, which takes more generation time than GeoFree [42]. LookOutside utilizes a pretrained encoder-decoder in GeoFree [42] for mapping the images to tokens. We adopt the official code for implementation ⁷.

B.3 Architectural Details

Encoder The channel dimension C of f_0 is set to 256, and all positional encoding layers embed into 32 channels. Thus, we first apply MLP-layers to embed C -dimensional input features for ISAB and LSA layers, where each MLP-layer takes $(C + 32)$ -dimensional features and outputs C -dimensional features. For a global set attention block, we first define a MAB (Multihead Attention Block) as:

$$\begin{aligned} \text{Attention}(Q, K, V) &= \text{Softmax}\left(\frac{QK^T}{\sqrt{d_{\text{head}}}}\right)V, \\ H &= \text{LayerNorm}(X + \text{Attention}(X, Y, Y)), \\ \text{MAB}(X, Y) &= \text{LayerNorm}(H + rFF(H)), \end{aligned} \quad (5)$$

where rFF denotes any row-wise feed-forward layer, and we use the same rFF in [21]. Then, using two MABs and m inducing points $I \in \mathbb{R}^{m \times C}$, we define the global set attention for n points as:

$$\begin{aligned} \text{ISAB}_m(X) &= \text{MAB}(X, G) \in \mathbb{R}^{n \times C}, \\ \text{where } G &= \text{MAB}(I, X) \in \mathbb{R}^{m \times C}. \end{aligned} \quad (6)$$

Note that, we compute the global set attention for $n = \frac{H}{4} \cdot \frac{W}{4}$ points, and fix $m = 32$. Moreover, in the LSA layer, we fix local window size $r = 5$ considering the previous point transformer networks where Point Transformer [59] uses 32 neighbors, and Fast Point Transformer [35] set local window size as 3 or 5. Finally, we apply Mix-FFN [54] to extract the i -th output point feature of the encoder f_i as:

$$\begin{aligned} f_i &= \text{Mix-FFN}(X_i) = \text{MLP}(\text{GELU}(\text{CONV}_{3 \times 3}(\text{MLP}(X_i)))) + X_i, \\ \text{where } X_i &= f_{i-1} + g_{\text{global}}^i + g_{\text{local}}^i. \end{aligned} \quad (7)$$

⁴<https://github.com/CompVis/geometry-free-view-synthesis>

⁵https://github.com/google-research/google-research/tree/master/infinite_nature

⁷<https://github.com/xrenaa/Look-Outside-Room>

Rendering Module We first illustrate the axis-angle notation, which is used for the implicit renderer. Axis-angle notation consists of *normalized axis*, i.e., a normalized vector along the axis is not changed by the rotation, and *angle*, i.e., the amount of rotation about that axis. We use a standard method that defines the eigenvector \mathbf{u} of the rotation matrix by using the property that $R - R^T$ is a skew-symmetric matrix as:

$$[\mathbf{u}]_X \equiv (R - R^T), \text{ i.e., } \mathbf{u} = [r_{32} - r_{23}, r_{13} - r_{31}, r_{21} - r_{12}]^T, \quad (8)$$

where r_{ij} is the element of R located at the i -th row and the j -th column. We can also calculate the rotation angle θ from the relationship between the norm of eigenvector $\|\mathbf{u}\|$ and the trace of the rotation matrix $\text{tr}(R)$. Following the existing theorem [9, 45], the rotation angle θ is derived as:

$$\theta = \arctan\left(\frac{\|\mathbf{u}\|}{\text{tr}(R) - 1}\right). \quad (9)$$

This notation often fails when the camera rotates near 180° ; however, we do not cover such an extreme movement of the camera. With a translation vector t , seven pose parameters (i.e., $(\frac{\mathbf{u}}{\|\mathbf{u}\|}, \theta, t)$) are processed into δ_{pos} , and then added to all output tokens of the overlapping patch embedding layer. Also, for both renderers, we use the MAB(Z, Z) described in Eq. 5 as transformer blocks for input feature Z , with MiX-FFN [54] as the feed-forward layer.

C Additional Results

C.1 Quantitative Results

PSNR measured for reprojected regions. To clarify the performance of preserving seen contents, we evaluate the PSNR only for reprojected pixels; the metric is denoted as *PSNR-vis*. Table 7 and Table 8 show the PSNR-vis for RealEstate10K [61] and ACID [24], respectively. Recent explicit methods [24, 41, 53] perform better than recent implicit methods [40, 42], which confirms that explicit methods better preserve the seen contents than implicit methods. Note that our method consistently achieves the highest PSNR-vis for all splits, outperforming previous methods by a large margin.

Table 7: PSNR-vis on RealEstate10K [61].

| Methods | PSNR-vis \uparrow | | | |
|--------------------------------|---------------------|--------------|--------------|--------------|
| | Small | Medium | Large | Average |
| Tatarchenko <i>et al.</i> [49] | 11.16 | 10.75 | 10.70 | 10.87 |
| Viewappearance [60] | 12.39 | 12.89 | 12.50 | 12.59 |
| SynSin [53] | 15.67 | 15.46 | 14.72 | 15.28 |
| SynSin-6x [53] | 15.43 | 15.54 | 14.92 | 15.30 |
| PixelSynth [41] | 15.62 | 15.60 | 14.64 | 15.29 |
| GeoFree [42] | 14.89 | 14.37 | 13.60 | 14.29 |
| LookOutside [40] | 12.78 | 13.13 | 12.54 | 12.82 |
| ours | 16.94 | 15.97 | 15.36 | 16.09 |

Table 8: PSNR-vis on ACID [24].

| Methods | PSNR-vis \uparrow | | | |
|--------------------------------|---------------------|--------------|--------------|--------------|
| | Small | Medium | Large | Average |
| Tatarchenko <i>et al.</i> [49] | 14.53 | 14.34 | 14.62 | 14.50 |
| Viewappearance [60] | 14.66 | 13.76 | 13.22 | 13.88 |
| SynSin [53] | 18.05 | 17.16 | 17.32 | 17.51 |
| InfNat [24] (1-step) | 16.97 | 15.74 | 15.24 | 15.98 |
| InfNat [24] (5-step) | 15.76 | 15.44 | 15.62 | 15.61 |
| PixelSynth [41] | 17.61 | 16.22 | 15.32 | 16.38 |
| GeoFree [42] | 15.26 | 14.86 | 14.67 | 14.93 |
| ours | 18.17 | 17.58 | 17.88 | 17.88 |

More Explorations of the Transformation Similarity Loss As we consistently mention the balance of the two renderers, we further explore the case where the norms of h_e and h_i are the same. Consequently, we use a ℓ_1 -loss instead of the negative cosine similarity loss to strengthen the coupling between the implicit renderer and the explicit renderer. Table 9 shows that tight bridging between two renderers degrades the generation power. Since the two renderers learn the different 3D scene representations for novel view synthesis, constraining h_i and h_e exactly the same causes a conflict in learning representations.

We also analyze the effect of the transformation similarity loss compared to using the out-of-view mask as an additional input for the decoder. If the out-of-view mask \mathbf{O} is concatenated with h_i and h_e , the decoder can learn to fuse the rendered feature h_i and h_e without our transformation similarity loss. As shown in Table 10, additional mask information achieves slight improvements for PSNR-vis, but the improvements in FID are negligible considering that it takes up a little more memory. Note that two renderers without our transformation similarity loss do not sufficiently represent semantic information, although additional mask information is used. On the other side, our method achieves significant performance improvement in both metrics while using the same memory as our method trained without L_{ts} .

Table 9: **Ablation Study on the Similarity Operation in L_{ts} .** PSNRs and FID are measured on RealEstate10K [61]. Note that the strict coupling between h_i and h_e reduces the generation performance in both PSNR and FID.

| Operation Type | Small | | | Medium | | | Large | | |
|----------------|---------------------|---------------------|------------------|---------------------|---------------------|------------------|---------------------|---------------------|------------------|
| | PSNR-vis \uparrow | PSNR-all \uparrow | FID \downarrow | PSNR-vis \uparrow | PSNR-all \uparrow | FID \downarrow | PSNR-vis \uparrow | PSNR-all \uparrow | FID \downarrow |
| ℓ_1 -loss | 16.43 | 15.46 | 42.21 | 15.66 | 14.47 | 44.97 | 15.11 | 13.72 | 55.18 |
| $-S_c(\cdot)$ | 16.94 | 15.87 | 32.42 | 15.97 | 14.65 | 33.04 | 15.36 | 13.83 | 35.26 |

Table 10: **Effects of the transformation similarity loss.** PSNRs and FID are measured on RealEstate10K [61]. Our transformation similarity loss is more effective than just using the out-of-view mask as an additional input of the decoder.

| Operation Type | Small | | | Medium | | | Large | | |
|----------------------------|---------------------|---------------------|------------------|---------------------|---------------------|------------------|---------------------|---------------------|------------------|
| | PSNR-vis \uparrow | PSNR-all \uparrow | FID \downarrow | PSNR-vis \uparrow | PSNR-all \uparrow | FID \downarrow | PSNR-vis \uparrow | PSNR-all \uparrow | FID \downarrow |
| No L_{ts} | 16.55 | 15.41 | 35.52 | 15.86 | 14.42 | 38.10 | 15.30 | 13.57 | 47.74 |
| $\mathbf{O}(p)$ as feature | 16.86 | 15.23 | 34.74 | 15.92 | 14.51 | 36.10 | 15.36 | 13.31 | 46.43 |
| ours | 16.94 | 15.87 | 32.42 | 15.97 | 14.65 | 33.04 | 15.36 | 13.83 | 35.26 |

Effects of the Adversarial Loss Since we use a different adversarial loss compared to SynSin [53], we further conducted an ablation study on the effect of the adversarial loss. Table 11 shows our adversarial loss improves the generation power of SynSin, but it is still a worse FID score than our method. We confirm that our method is not just boosted with a more powerful adversarial loss. Our architecture advances bridging explicit and implicit geometric transformations with transformation similarity loss contributes significantly to performance gain.

Also, the new GAN loss does not solve the seesaw problem as it improves SynSin in FID by sacrificing PSNR-vis. Explicit methods still have room for improvement in completing out-of-view regions, but more advanced generative models cannot solve the seesaw problem. Note that our bridging scheme and the transformation similarity loss are necessary to mitigate the seesaw problem.

Table 11: **Effects of the adversarial loss.** PSNRs and FID are measured on RealEstate10K [61].

| Operation Type | Small | | | Medium | | | Large | | |
|------------------------|---------------------|---------------------|------------------|---------------------|---------------------|------------------|---------------------|---------------------|------------------|
| | PSNR-vis \uparrow | PSNR-all \uparrow | FID \downarrow | PSNR-vis \uparrow | PSNR-all \uparrow | FID \downarrow | PSNR-vis \uparrow | PSNR-all \uparrow | FID \downarrow |
| SynSin | 15.67 | 15.38 | 41.75 | 15.46 | 14.88 | 43.06 | 14.72 | 13.96 | 61.67 |
| SynSin + our L_{adv} | 15.45 | 15.23 | 40.43 | 15.31 | 14.88 | 39.13 | 14.51 | 13.98 | 54.27 |
| ours | 16.94 | 15.87 | 32.42 | 15.97 | 14.65 | 33.04 | 15.36 | 13.83 | 35.26 |

C.2 Qualitative Results

We further evaluate our method on different sizes of viewpoint changes as shown in Fig. 7 and Fig. 8. We also visualize additional qualitative results in Fig. 9. Note that our method synthesizes novel views consistent with I_{ref} and realistic out-of-view regions, regardless of the view change.

D Discussion

Failure Cases Since we train the depth estimation network in a self-supervised manner, some reprojected regions can be mismatched with the target image due to various reasons (e.g., occlusion and textureless regions), reducing the accuracy of explicitly rendered features. Most mismatches are corrected by balancing with the implicit renderer, but occlusions in textureless regions may create some artifacts in the generated image.

Limitations and Future Works As many possible target images can be consistent with the reference image and the relative camera pose, a probabilistic framework may generate better novel views than deterministic models. We will explore how to combine our bridging scheme and recent probabilistic frameworks in future work.

Potential Social Negative Impact Moving the camera from a photograph with single-image view synthesis can be used to affect privacy adversely. As the model trained on specific data can be biased, training data must be carefully selected.

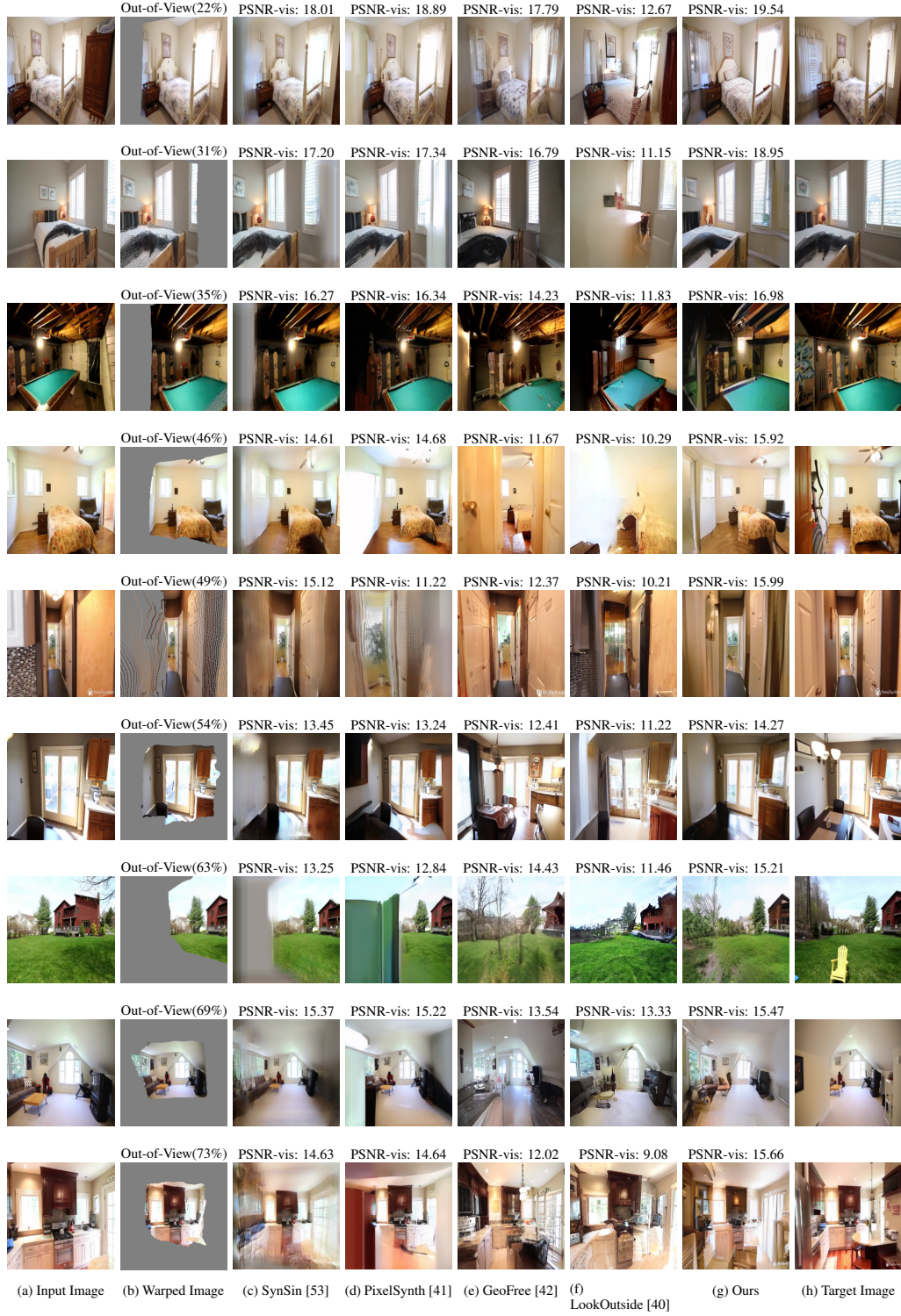


Figure 7: Qualitative Results on RealEstate10K [61].

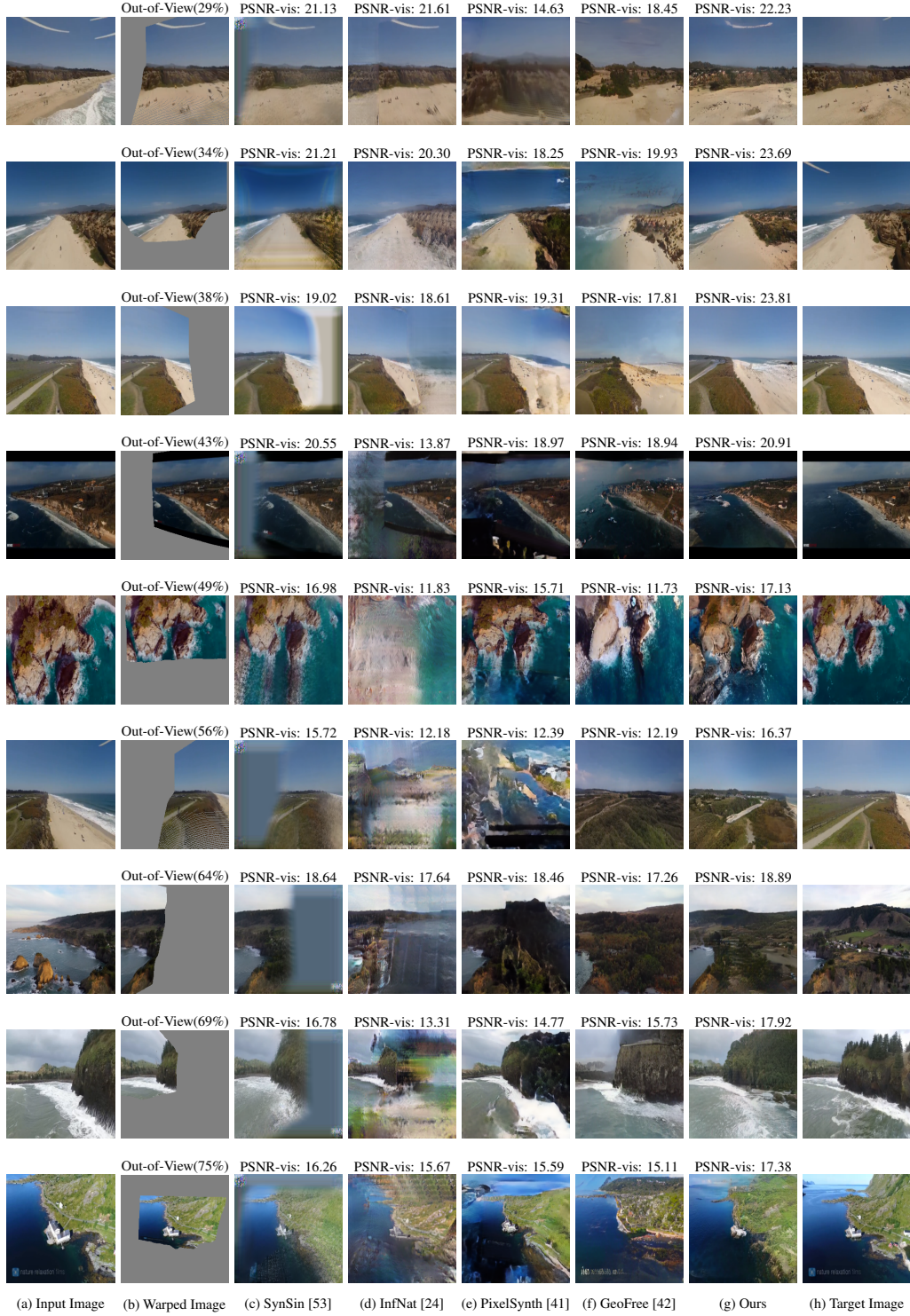


Figure 8: **Qualitative Results on ACID [24]**. For InfNat [24], we report examples with higher PSNR-vis scores in either 1-step or 5-step variants.

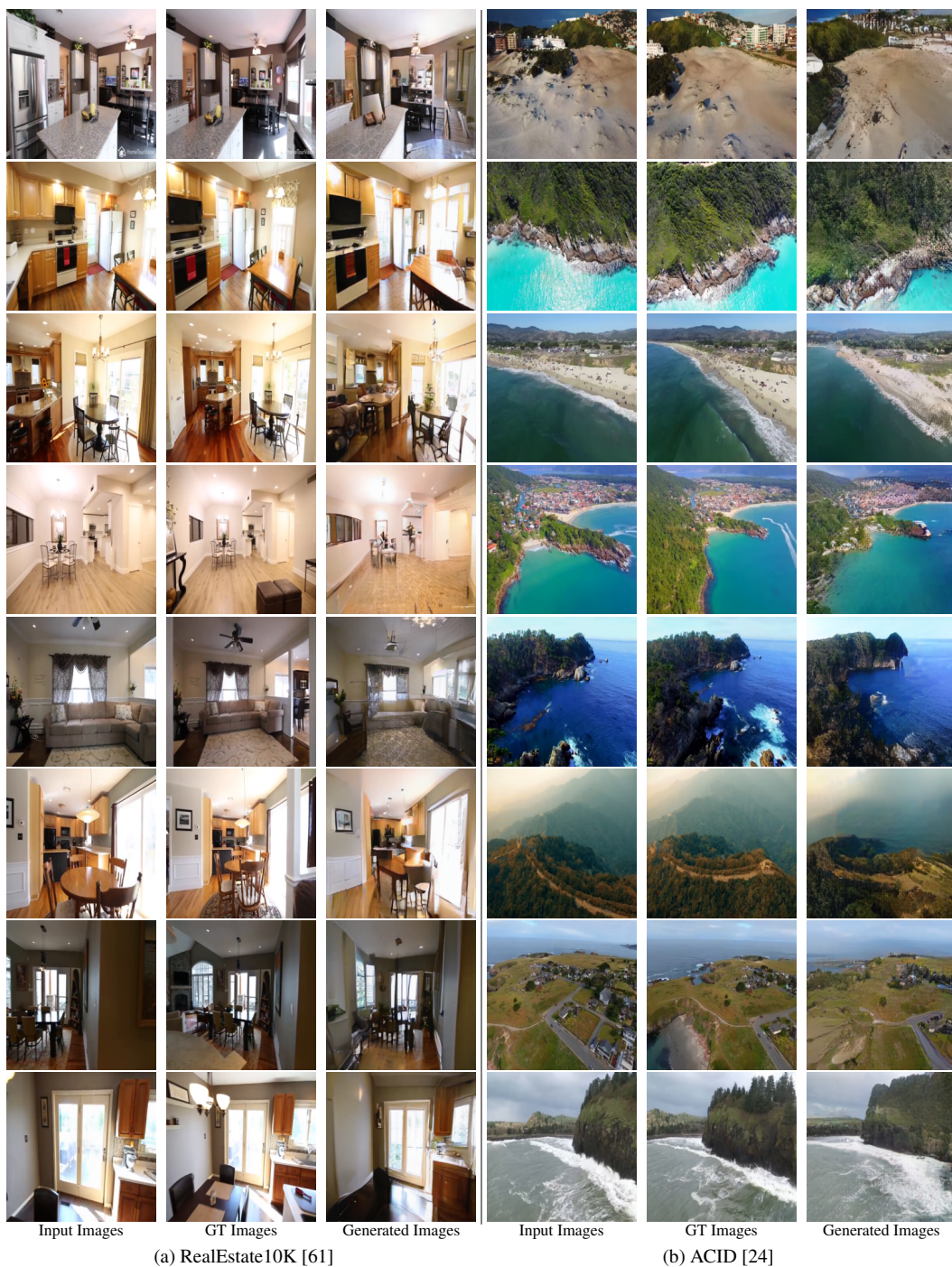


Figure 9: **Additional Qualitative Results.**

References

- [1] Kara-Ali Aliev, Artem Sevastopolsky, Maria Kolos, Dmitry Ulyanov, and Victor Lempitsky. Neural point-based graphics. In *European Conference on Computer Vision*, pages 696–712. Springer, 2020.
- [2] Wenbo Bao, Wei-Sheng Lai, Chao Ma, Xiaoyun Zhang, Zhiyong Gao, and Ming-Hsuan Yang. Depth-aware video frame interpolation. In *Proceedings of the IEEE/CVF Conference on Computer Vision and Pattern Recognition*, pages 3703–3712, 2019.
- [3] Andrew Brock, Jeff Donahue, and Karen Simonyan. Large scale gan training for high fidelity natural image synthesis. *arXiv preprint arXiv:1809.11096*, 2018.
- [4] Shenchang Eric Chen and Lance Williams. View interpolation for image synthesis. In *Proceedings of the 20th annual conference on Computer graphics and interactive techniques*, pages 279–288, 1993.
- [5] Xu Chen, Jie Song, and Otmar Hilliges. Monocular neural image based rendering with continuous view control. In *Proceedings of the IEEE/CVF International Conference on Computer Vision*, pages 4090–4100, 2019.
- [6] Paul Debevec, Yizhou Yu, and George Borshukov. Efficient view-dependent image-based rendering with projective texture-mapping. In *Eurographics Workshop on Rendering Techniques*, pages 105–116. Springer, 1998.
- [7] Paul E Debevec, Camillo J Taylor, and Jitendra Malik. Modeling and rendering architecture from photographs: A hybrid geometry-and image-based approach. In *Proceedings of the 23rd annual conference on Computer graphics and interactive techniques*, pages 11–20, 1996.
- [8] Jacob Devlin, Ming-Wei Chang, Kenton Lee, and Kristina Toutanova. Bert: Pre-training of deep bidirectional transformers for language understanding. *arXiv preprint arXiv:1810.04805*, 2018.
- [9] James Diebel. Representing attitude: Euler angles, unit quaternions, and rotation vectors. 2006.
- [10] Alexey Dosovitskiy, Lucas Beyer, Alexander Kolesnikov, Dirk Weissenborn, Xiaohua Zhai, Thomas Unterthiner, Mostafa Dehghani, Matthias Minderer, Georg Heigold, Sylvain Gelly, et al. An image is worth 16x16 words: Transformers for image recognition at scale. *arXiv preprint arXiv:2010.11929*, 2020.
- [11] Patrick Esser, Robin Rombach, and Bjorn Ommer. Taming transformers for high-resolution image synthesis. In *Proceedings of the IEEE/CVF Conference on Computer Vision and Pattern Recognition*, pages 12873–12883, 2021.
- [12] John Flynn, Michael Broxton, Paul Debevec, Matthew DuVall, Graham Fyffe, Ryan Overbeck, Noah Snavely, and Richard Tucker. Deepview: View synthesis with learned gradient descent. In *Proceedings of the IEEE/CVF Conference on Computer Vision and Pattern Recognition*, pages 2367–2376, 2019.
- [13] Clément Godard, Oisín Mac Aodha, and Gabriel J Brostow. Unsupervised monocular depth estimation with left-right consistency. In *Proceedings of the IEEE Conference on Computer Vision and Pattern Recognition*, pages 270–279, 2017.
- [14] Steven J Gortler, Radek Grzeszczuk, Richard Szeliski, and Michael F Cohen. The lumigraph. In *Proceedings of the 23rd annual conference on Computer graphics and interactive techniques*, pages 43–54, 1996.
- [15] Meng-Hao Guo, Jun-Xiong Cai, Zheng-Ning Liu, Tai-Jiang Mu, Ralph R Martin, and Shi-Min Hu. Pct: Point cloud transformer. *Computational Visual Media*, 7(2):187–199, 2021.
- [16] Peter Hedman, Julien Philip, True Price, Jan-Michael Frahm, George Drettakis, and Gabriel Brostow. Deep blending for free-viewpoint image-based rendering. *ACM Transactions on Graphics (TOG)*, 37(6):1–15, 2018.
- [17] Martin Heusel, Hubert Ramsauer, Thomas Unterthiner, Bernhard Nessler, and Sepp Hochreiter. Gans trained by a two time-scale update rule converge to a local nash equilibrium. *Advances in neural information processing systems*, 30, 2017.
- [18] Yuxin Hou, Arno Solin, and Juho Kannala. Novel view synthesis via depth-guided skip connections. In *Proceedings of the IEEE/CVF Winter Conference on Applications of Computer Vision*, pages 3119–3128, 2021.
- [19] Ronghang Hu, Nikhila Ravi, Alexander C Berg, and Deepak Pathak. Worldsheet: Wrapping the world in a 3d sheet for view synthesis from a single image. In *Proceedings of the IEEE/CVF International Conference on Computer Vision*, pages 12528–12537, 2021.

- [20] Satoshi Iizuka, Edgar Simo-Serra, and Hiroshi Ishikawa. Globally and locally consistent image completion. *ACM Transactions on Graphics (ToG)*, 36(4):1–14, 2017.
- [21] Juho Lee, Yoonho Lee, Jungtaek Kim, Adam Kosiorek, Seungjin Choi, and Yee Whye Teh. Set transformer: A framework for attention-based permutation-invariant neural networks. In *International Conference on Machine Learning*, pages 3744–3753. PMLR, 2019.
- [22] Marc Levoy and Pat Hanrahan. Light field rendering. In *Proceedings of the 23rd annual conference on Computer graphics and interactive techniques*, pages 31–42, 1996.
- [23] Jae Hyun Lim and Jong Chul Ye. Geometric gan. *arXiv preprint arXiv:1705.02894*, 2017.
- [24] Andrew Liu, Richard Tucker, Varun Jampani, Ameesh Makadia, Noah Snavely, and Angjoo Kanazawa. Infinite nature: Perpetual view generation of natural scenes from a single image. In *Proceedings of the IEEE/CVF International Conference on Computer Vision*, pages 14458–14467, 2021.
- [25] Xinhai Liu, Zhizhong Han, Yu-Shen Liu, and Matthias Zwicker. Point2sequence: Learning the shape representation of 3d point clouds with an attention-based sequence to sequence network. In *Proceedings of the AAAI Conference on Artificial Intelligence*, volume 33, pages 8778–8785, 2019.
- [26] Stephen Lombardi, Tomas Simon, Jason Saragih, Gabriel Schwartz, Andreas Lehrmann, and Yaser Sheikh. Neural volumes: Learning dynamic renderable volumes from images. *arXiv preprint arXiv:1906.07751*, 2019.
- [27] Ilya Loshchilov and Frank Hutter. Sgdr: Stochastic gradient descent with warm restarts. *arXiv preprint arXiv:1608.03983*, 2016.
- [28] Ilya Loshchilov and Frank Hutter. Decoupled weight decay regularization. *arXiv preprint arXiv:1711.05101*, 2017.
- [29] Ricardo Martin-Brualla, Rohit Pandey, Shuoran Yang, Pavel Pidlypenskyi, Jonathan Taylor, Julien Valentin, Sameh Khamis, Philip Davidson, Anastasia Tkach, Peter Lincoln, et al. Lookingood: Enhancing performance capture with real-time neural re-rendering. *arXiv preprint arXiv:1811.05029*, 2018.
- [30] Moustafa Meshry, Dan B Goldman, Sameh Khamis, Hugues Hoppe, Rohit Pandey, Noah Snavely, and Ricardo Martin-Brualla. Neural rerendering in the wild. In *Proceedings of the IEEE/CVF Conference on Computer Vision and Pattern Recognition*, pages 6878–6887, 2019.
- [31] Ben Mildenhall, Pratul P Srinivasan, Matthew Tancik, Jonathan T Barron, Ravi Ramamoorthi, and Ren Ng. Nerf: Representing scenes as neural radiance fields for view synthesis. In *European conference on computer vision*, pages 405–421. Springer, 2020.
- [32] Simon Niklaus and Feng Liu. Softmax splatting for video frame interpolation. In *Proceedings of the IEEE/CVF Conference on Computer Vision and Pattern Recognition*, pages 5437–5446, 2020.
- [33] David Novotny, Ben Graham, and Jeremy Reizenstein. Perspectivenet: A scene-consistent image generator for new view synthesis in real indoor environments. *Advances in Neural Information Processing Systems*, 32, 2019.
- [34] Kyle Olszewski, Sergey Tulyakov, Oliver Woodford, Hao Li, and Linjie Luo. Transformable bottleneck networks. In *Proceedings of the IEEE/CVF International Conference on Computer Vision*, pages 7648–7657, 2019.
- [35] Chunghyun Park, Yoonwoo Jeong, Minsu Cho, and Jaesik Park. Fast point transformer. *arXiv preprint arXiv:2112.04702*, 2021.
- [36] Taesung Park, Ming-Yu Liu, Ting-Chun Wang, and Jun-Yan Zhu. Semantic image synthesis with spatially-adaptive normalization. In *Proceedings of the IEEE/CVF conference on computer vision and pattern recognition*, pages 2337–2346, 2019.
- [37] Alec Radford, Jeffrey Wu, Rewon Child, David Luan, Dario Amodei, Ilya Sutskever, et al. Language models are unsupervised multitask learners. *OpenAI blog*, 1(8):9, 2019.
- [38] René Ranftl, Katrin Lasinger, David Hafner, Konrad Schindler, and Vladlen Koltun. Towards robust monocular depth estimation: Mixing datasets for zero-shot cross-dataset transfer. *IEEE transactions on pattern analysis and machine intelligence*, 2020.
- [39] Ali Razavi, Aaron Van den Oord, and Oriol Vinyals. Generating diverse high-fidelity images with vq-vae-2. *Advances in neural information processing systems*, 32, 2019.

- [40] Xuanchi Ren and Xiaolong Wang. Look outside the room: Synthesizing a consistent long-term 3d scene video from a single image. In *Proceedings of the IEEE/CVF Conference on Computer Vision and Pattern Recognition (CVPR)*, 2022.
- [41] Chris Rockwell, David F Fouhey, and Justin Johnson. Pixelsynth: Generating a 3d-consistent experience from a single image. In *Proceedings of the IEEE/CVF International Conference on Computer Vision*, pages 14104–14113, 2021.
- [42] Robin Rombach, Patrick Esser, and Björn Ommer. Geometry-free view synthesis: Transformers and no 3d priors. In *Proceedings of the IEEE/CVF International Conference on Computer Vision*, pages 14356–14366, 2021.
- [43] Axel Sauer, Kashyap Chitta, Jens Müller, and Andreas Geiger. Projected gans converge faster. *Advances in Neural Information Processing Systems*, 34, 2021.
- [44] Steven M Seitz, Brian Curless, James Diebel, Daniel Scharstein, and Richard Szeliski. A comparison and evaluation of multi-view stereo reconstruction algorithms. In *2006 IEEE computer society conference on computer vision and pattern recognition (CVPR'06)*, volume 1, pages 519–528. IEEE, 2006.
- [45] Stanley W Shepperd. Quaternion from rotation matrix. *Journal of guidance and control*, 1(3):223–224, 1978.
- [46] Vincent Sitzmann, Justus Thies, Felix Heide, Matthias Nießner, Gordon Wetzstein, and Michael Zollhofer. Deepvoxels: Learning persistent 3d feature embeddings. In *Proceedings of the IEEE/CVF Conference on Computer Vision and Pattern Recognition*, pages 2437–2446, 2019.
- [47] Pratul P Srinivasan, Tongzhou Wang, Ashwin Sreelal, Ravi Ramamoorthi, and Ren Ng. Learning to synthesize a 4d rgbd light field from a single image. In *Proceedings of the IEEE International Conference on Computer Vision*, pages 2243–2251, 2017.
- [48] Pratul P Srinivasan, Richard Tucker, Jonathan T Barron, Ravi Ramamoorthi, Ren Ng, and Noah Snavely. Pushing the boundaries of view extrapolation with multiplane images. In *Proceedings of the IEEE/CVF Conference on Computer Vision and Pattern Recognition*, pages 175–184, 2019.
- [49] Maxim Tatarchenko, Alexey Dosovitskiy, and Thomas Brox. Multi-view 3d models from single images with a convolutional network. In *European Conference on Computer Vision*, pages 322–337. Springer, 2016.
- [50] Shubham Tulsiani, Richard Tucker, and Noah Snavely. Layer-structured 3d scene inference via view synthesis. In *Proceedings of the European Conference on Computer Vision (ECCV)*, pages 302–317, 2018.
- [51] Ashish Vaswani, Noam Shazeer, Niki Parmar, Jakob Uszkoreit, Llion Jones, Aidan N Gomez, Łukasz Kaiser, and Illia Polosukhin. Attention is all you need. *Advances in neural information processing systems*, 30, 2017.
- [52] Qianqian Wang, Zhicheng Wang, Kyle Genova, Pratul P Srinivasan, Howard Zhou, Jonathan T Barron, Ricardo Martin-Brualla, Noah Snavely, and Thomas Funkhouser. Ibrnet: Learning multi-view image-based rendering. In *Proceedings of the IEEE/CVF Conference on Computer Vision and Pattern Recognition*, pages 4690–4699, 2021.
- [53] Olivia Wiles, Georgia Gkioxari, Richard Szeliski, and Justin Johnson. Synsin: End-to-end view synthesis from a single image. In *Proceedings of the IEEE/CVF Conference on Computer Vision and Pattern Recognition*, pages 7467–7477, 2020.
- [54] Enze Xie, Wenhai Wang, Zhiding Yu, Anima Anandkumar, Jose M Alvarez, and Ping Luo. Segformer: Simple and efficient design for semantic segmentation with transformers. *Advances in Neural Information Processing Systems*, 34, 2021.
- [55] Saining Xie, Sainan Liu, Zeyu Chen, and Zhuowen Tu. Attentional shapecontextnet for point cloud recognition. In *Proceedings of the IEEE Conference on Computer Vision and Pattern Recognition*, pages 4606–4615, 2018.
- [56] Jiancheng Yang, Qiang Zhang, Bingbing Ni, Linguo Li, Jinxian Liu, Mengdie Zhou, and Qi Tian. Modeling point clouds with self-attention and gumbel subset sampling. In *Proceedings of the IEEE/CVF Conference on Computer Vision and Pattern Recognition*, pages 3323–3332, 2019.
- [57] Alex Yu, Vickie Ye, Matthew Tancik, and Angjoo Kanazawa. pixelnerf: Neural radiance fields from one or few images. In *Proceedings of the IEEE/CVF Conference on Computer Vision and Pattern Recognition*, pages 4578–4587, 2021.

- [58] Kai Zhang, Gernot Riegler, Noah Snavely, and Vladlen Koltun. Nerf++: Analyzing and improving neural radiance fields. *arXiv preprint arXiv:2010.07492*, 2020.
- [59] Hengshuang Zhao, Li Jiang, Jiaya Jia, Philip HS Torr, and Vladlen Koltun. Point transformer. In *Proceedings of the IEEE/CVF International Conference on Computer Vision*, pages 16259–16268, 2021.
- [60] Tinghui Zhou, Shubham Tulsiani, Weilun Sun, Jitendra Malik, and Alexei A Efros. View synthesis by appearance flow. In *European conference on computer vision*, pages 286–301. Springer, 2016.
- [61] Tinghui Zhou, Richard Tucker, John Flynn, Graham Fyffe, and Noah Snavely. Stereo magnification: Learning view synthesis using multiplane images. *arXiv preprint arXiv:1805.09817*, 2018.
- [62] C Lawrence Zitnick, Sing Bing Kang, Matthew Uyttendaele, Simon Winder, and Richard Szeliski. High-quality video view interpolation using a layered representation. *ACM transactions on graphics (TOG)*, 23(3):600–608, 2004.